Zeitschrift für Physikalische Chemie, Bd. 206, S. 197–218 (1998)

Point Defects of Tephroite. I: The Electrical Conductivity of Mn_2SiO_4

By Christoph Stüber and Wolfgang Laqua

Institut für Anorganische und Analytische Chemie I, Justus-Liebig-Universität Gießen, Heinrich-Buff-Ring 58, D-35392 Gießen, Germany

Dedicated to Professor Hermann Schmalzried on the occasion of his 65th birthday

(Received March 25, 1997)

Olivin (Mn_2SiO_4) / Electrical conductivity / Point-defect equilibria

The electrical conductivity σ of single crystalline Mn_2SiO_4 (tephroite) grown from the melt, was investigated by impedance spectroscopy between 1101 and 1197 °C as function of oxygen activity within the range $\sim 10^{-16} \leq a_{O_2} \leq 0.21$ (air). Mn_2SiO_4 is n-conducting within the low and p-conducting within the high oxygen-activity regime, independent whether the sample are buffered against MnO or $MnSiO_3$.

Based on our experimental results we propose a point-defect model the majority defects of which are vacancies in the manganese sublattice V''_{Mn}, Mn^{3+}-ions on Si-lattice sites Mn'_{Si}, holes $h^{\bullet}$ ($\equiv Mn^{\bullet}_{Mn}$) and electrons e'.

Unlike Fe_2SiO_4 (fayalite), wherein according to thermogravimetric results of Nakamura and Schmalzried [1] associates $\{Fe^{\bullet}_{Fe}Fe'_{Si}\}^{\times}$ exist, our defect model works without postulating the analogous species $\{Mn^{\bullet}_{Mn}Mn'_{Si}\}^{\times}$ to exist in tephroite. We drew this conclusion from the 1/5.5-power law which is followed by our σ-a_{O_2}-plots measured on stoichiometric tephroite in the high-a_{O_2} regime, whereas Nakamura and Schmalzried derived an 1/5.0 power law from their measurements in the range of similar oxygen activities on likewise stoichiometric fayalite.

The equilibrium constants for formation reactions of the aforementioned defects, which emerged from our experiments were used to depict Kröger-Vink diagrams; they describe the dependence of defect concentrations on oxygen activities for both MnO resp. $MnSiO_3$ buffered tephroite.

1. Introduction

Manganese-orthosilicate, Mn_2SiO_4, otherwise known as the mineral tephroite, belongs to the olivine-type family. Its members crystallize with the oxygen ions in an approximately hexagonal-close packed array, whereas the cations occupy two types of octahedrally coordinated sites with different

point-group symmetry, designated M1 and M2 in the literature [2]. The rock forming olivine is a member of the solid-solution series between forsterite (Mg_2SiO_4) and fayalite (Fe_2SiO_4). Sometimes it contains tephroite as a minor third component. Olivine is a main constituent of the earth's upper mantle and determines to a large extend the mantle rheology. Because forsterite, fayalite and tephroite form solid solution series without any miscibility gap at elevated temperatures, the pure end members are rarely to be found in natural rock assemblages. Besides naturally occurring olivines there are well known examples of synthetically prepared compounds such as Co_2SiO_4 and Ni_2SiO_4, which also have an olivine-type structure.

Transport properties such as diffusion, electrical conductivity and creep behaviour of olivines are governed by their point-defect thermodynamics [3, 4]. Hence it is essential for an understanding of such properties to have exact knowledge of the main kind of point defects, their concentrations and dependencies from the independent thermodynamic variables.

Based on experimental results, available then from the literature, theoretical point-defect models have been developed for forsterite [5] and olivine [6–8]. The problem has been tackled more fundamentally by Nakamura and Schmalzried [1], who delt with point-defect thermodynamics of fayalite related to their thermogravimetric results on synthetic fayalite.

Ever since, conceptions of the foregoing authors have been widely used to explain mass-transport phenomena in olivine-type minerals and compounds. We refer to investigations of creep phenomena [9, 10], diffusion [11–15] and demixing in oxygen potential gradients [16–18].

Numerous investigations are known concerning the electrical conductivity of olivine-type compounds [19–33]. Reference is given here only to more or less recently published results, because some of the elder literature data are not quite unambiguous due to the fact that not all the independent thermodynamic variables were adequately fixed.

In this paper we report on the electrical conductivity of synthetic tephroite under both MnO buffered and $MnSiO_3$ buffered conditions as function of temperature (1097–1223 °C) and oxygen activity ($\sim 10^{-16}$–0.21). Our results will be analysed on the basis of Nakamura and Schmalzried's defect model for fayalite [1]. This model is made up of three types of point defects, two of them we are familiar with, namely (Kröger-Vink notation is used throughout) cationic vacancies V''_{Mn} and holes $h^{\bullet}$ ($\equiv Fe^{\bullet}_{Fe}$). However, as a most striking result of these author's data analysis it came out that a third majority defect exists in fayalite, that is the associated species $\{Fe^{\bullet}_{Fe}Fe'_{Si}\}^{x}$ containing a hole $Fe^{\bullet}_{Fe}$ and an Fe^{3+}-ion located on a Si-lattice site Fe'_{Si}.

Our discussion is focused on whether or not the existence of an analogous associate $\{Mn^{\bullet}_{Mn}Mn'_{Si}\}^{x}$ is consistent with our experimental results. As will be shown later, our point defect model for tephroite lacks such an associated species.

Some room will be given to a comparison of our results with those of Bai *et al.* [30], who investigated the electrical conductivity of tephroite single crystals under similar thermodynamic conditions as ours apart from the fact that our measurements have been extended to lower oxygen activities ($a_{O_2} = 10^{-16}$ in this work, $a_{O_2} = 10^{-10}$ in [30]).

2. Experimental techniques

2.1 Sample preparation

Mn_2SiO_4 was synthesized from manganese(II)oxalate, MnC_2O_4, and silicagel, SiO_2 (99.9%, Merck).

MnC_2O_4 was prepared from metallic manganese (99.9%, Riedel de Haën). The metal was solved in glacial acetic acid. The solution was diluted with the same amount of water whereupon $MnC_2O_4 \cdot 3\ H_2O$ (of light pink colour) was precipitated by adding a dilute solution of ammonium oxalate ($c = 2\ mol \cdot l^{-1}$) in excess (molar ratio 1.1 : 1) under stirring. The suspension formed was heated within 30 minutes up to the boiling point and was afterwards slowly cooled down to room temperature within 6 hours on a sand bath.

In the course of this procedure the trihydrated $MnC_2O_4 \cdot 3\ H_2O$ loses one mole of water, thereby transforming to colourless $MnC_2O_4 \cdot 2\ H_2O$, which was filtered off, washed and dried. The dihydrated oxalate must be held at 150 °C in air for some hours to remove the remaining water. The completeness of the decomposition reaction under these conditions was proved in an extra run by thermogravimetric analysis. The Mn-content of the as-prepared manganese oxalate was controlled by wet-chemical analysis. The silicagel was dried at 250 °C in air until weight constancy was achieved.

Then both the educt components MnC_2O_4 and SiO_2 were finely ground for 2 hours in an agate mortar under methanol in proportions according to the formula $(Mn,Si)_{3-3\delta}O_4$ with $n(MnO)/n(SiO_2) = 1.774$; 2.00 (stoichiometric) and 2.061. Based on the results of Sandner and Laqua [34] the ratio of the mole numbers of MnO and SiO_2 was chosen in such a way that saturation of the Mn_2SiO_4 lattice with MnO at one side of the small homogeneity range and with $MnSiO_3$ at the other side was definitely established (see below).

After evaporation of the methanol and subsequent drying, the powder mixture was hydrostatically pressed into small pellets (10 mm diameter, 15 mm high; pressure 1.5 kbar) within a stainless-steel matrice and prereacted at 600 °C for 4 h and at 1100 °C for 6 h in a CO/CO_2 (10 : 90) atmosphere. The pellets were ground again and heated at 1400 °C for 2 h ($a_{O_2} = 5 \cdot 10^{-11}$) in a finger-like Pt-crucible, where they formed a nearly transparent melt.

After all the gas bubbles within the melt had disappeared, the crystallization was initiated by pulling the crucible down the vertically operating SiC-tube furnace at a speed of 2 mm/h. At 1200 °C the crucible movement was interrupted for 8 hours in order to let the solidified melt mechanically relax. After the Pt crucible had reached room temperature the platinum could easily be detached from the tephroite oligocrystal, which had been formed during the crystallization process. On average such oligocrystals contained 5–7 smaller single crystals within an overall crystal volume of about 1 cm^3 (the density of the oligocrystals reached 96–98% of the theoretical value).

Samples with an SiO_2-excess ($n(Mn)/n(Si) < 2$) were found to be dark greyish, the ones with an MnO-excess ($n(Mn)/n(Si) > 2$) were of light-green colour, whereas samples with a stoichiometric composition ($n(Mn)/n(Si) = 2$) appeared to be brownish.

It was established by electron-microprobe analysis and optical microscopy that samples with SiO_2-excess contained small amounts of $MnSiO_3$, whereas samples with a SiO_2-deficit contained small amounts of MnO as second phase, which proved that both the thermodynamic component activities a_{MnSiO_3} and a_{MnO} were definitely fixed.

2.2 Electrical conductivity measurements

For measurements of the electrical conductivity we used an impedance analyzer (Hewlett-Packard, model 4192A), which operates in the range from 5 Hz to 1 MHz. The tephroite oligocrystals were cut into small bars with a diamond saw and ground to small rods (7 mm in diameter, 4–7 mm in length) by using a diamond wheel. The polishing was achieved with diamond paste of different grain size down to 0.25 µm. The samples were then ultrasonically cleaned in water for some minutes. Both opposite surfaces of the cylindrical sample were sputtered with platinum. Afterwards two platinum electrodes (Mn-presaturated), cut from a 50 µm thick platinum sheet were attached to these platinum coated surfaces and held together by spring loading.

We fixed the oxygen activity with CO/CO_2-mixtures in the lower activity range ($a_{O_2} < 10^{-4}$) and with Ar (purified over Ti sponge)/O_2 mixtures in the upper activity range ($a_{O_2} \geq 10^{-4}$); the temperature range was 1101 to 1197 °C. All gases were of chemical grade. The time we had to wait until a new equilibrium state has been reached after changing the gas composition varied between 2 h at high activities and 8 h at low activities. All measurements were performed from lower to higher oxygen activities. We did not perform measurements from higher to lower activities because it took to long a time especially in the low activity regime to reach a new equilibrium state after changing the gas composition (~2–3 days). The temperature was altered in 10 °C steps; each new equilibrium state was

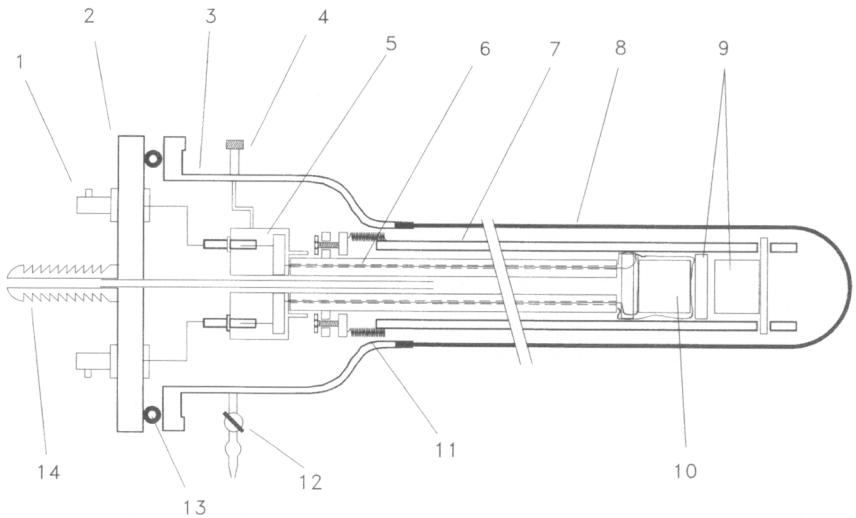

Fig. 1. Sketch of the experimental equipment for the electrical conductivity measurements on tephroite (not to scale). 1) BNC connections to impedance analyser. 2) Aluminum front sheet. 3) Glas flange. 4) Socket for thermocouple connections. 5) Measuring head. 6) Seven-hole corundum rod, bearing the Pt/Pt-10%-Rh thermocouple. 7) Inner corundum tube with sew-out slit allowing sample access. 8) Outer corundum protecting tube (one-side closed). 9) Corundum sheets and corundum block (sample holder). 10) Sample. 11) Adjustable stainless steel springs. 12) Gas outlet. 13) O-ring seal. 14) Gas inlet.

reached after about 20 minutes. Measurements were performed with rising and falling temperatures. No differences could be detected for both such runs.

Oxygen activities were controlled with a solid-state galvanic cell (CaO-stabilized zirconia). The sensor was installed outside the impedance cell in an extra furnace placed in the immediate vicinity of the impedance measuring device to keep the distance the gas has to cover as short as possible. With a three-path valve it was feasible to consecutively and alternatively monitoring the oxygen activity at the inlet and the outlet of the cell equipment, thus immediately becoming aware of oxygen leaks in the corundum tube that surrounded the impedance cell. All gas leading tubes were made of copper. The single parts of the copper tubes, which connected the components of the gas-supply system (two gas containers, two high accuracy gas-mixing pumps, Woesthoff, Germany, reliance $\pm 1\%$), the impedance measuring cell and the a_{O_2}-monitoring device were cold welded via fittings to minimize gas leaks at the connections as far as possible.

A sketch of our impedance measuring assembly is shown in Fig. 1 (not so scale).

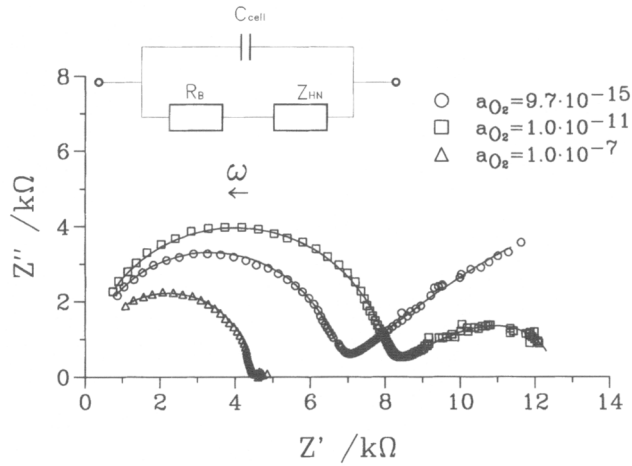

Fig. 2. Experimental and calculated (full lines) impedance spectra (5 Hz−1 MHz) of synthetic tephroite for different oxygen activities at 1191 °C. The MnO activity is fixed at $a_{MnO} = 1$. The equivalent circuit is depicted as insert (C_{cell} = cell capacitance, R_B = bulk resistivity, Z_{HN} = Havriliak-Negami element).

The high-temperature tube furnace was equipped with a SiC heating element. The temperature was adjusted with a PID-regulator (Type 820, Eurotherm, Germany). An RS 232 interface was used to computer regulate and control the furnace temperature. The index value of the temperature could be given with a resolution of 1 °C. The fluctuation of temperature at the index value was less than ±0.2 °C. The thermo-emf was measured against a 50 °C-cold junction.

The recorded impedance spectra were analysed with the programme LEVM [35] in the version, which is continuously actualized by the authors [36] and which is available on request. In general, the spectra feature two semicircles; an example is given in Fig. 2. However, the high-frequency semicircle can only be seen at $a_{O_2} = 1 \cdot 10^{-11}$ in Fig. 2. To make the full low-frequency semicircle visible in case of $a_{O_2} = 9.7 \cdot 10^{-11}$, one has to reduce the scale, whereas in case of $a_{O_2} = 1.0 \cdot 10^{-7}$ the scale has to be enlarged. Investigations with systematically varied cell dimensions were not performed. However, in one of our runs we considerably changed the cell dimensions compared to the values described in the foregoing section. It turned out that the specific electrical conductivity has not altered, giving further support to our interpretation of the experimental data on the basis of an equivalent circuit which is outlined below.

We attribute the high-frequency semicircle to the bulk resistance, whereas the interface resistance is mirrored by the low-frequency semicircle. The interface resistance, estimated under conditions of increasing and decreasing

temperature shows a distinct hysteresis, which is helpful to separate interface and bulk properties. Beside that part of an interface resistance which is usually located at the electrode/sample phase boundary we have to deal with a second part, which originates from a thin some μm thick rhodonite layer, formed at the tephroite-platinum electrode interface despite the fact that Mn-presaturated platinum foils were used as electrode material.

As can be seen from Fig. 2, the interface resistance increases drastically with decreasing oxygen activities. Apparently, the Mn formed according to the reaction

$$Mn_2SiO_4 = Mn + MnSiO_3 + 1/2\ O_2$$

diffuses through the Mn-presaturated platinum foil to the alumina support at the outer electrode interface where it reacts to manganese spinel $MnAl_2O_4$; this process seems to be strongly influenced by the oxygen activity. To make sure that the tephroite samples still remained in the buffered state during the impedance measurements despite the fact that thin rhodonite layers are formed at the electrode interface, we investigated each tephroite sample after an experimental run with the electron microprobe. In all cases, traces of MnO resp. $MnSiO_3$ buffer were detectable within the tephroite matrix. From the shape of the low frequency semicircle we conclude that the permeation of the charge carriers through the $MnSiO_3$/Pt(Mn) interface is diffusion controlled. Within the rhodonite layer the movement of electronic charge carriers in the alternating electrical field is superimposed by a diffusion of Mn^{2+}-ions in the chemical activity gradient, which is established even unknown within the rhodonite layer. This in turn leads to an asymmetrical dispersion of the relaxation times, which can be described by use of the empirical Havriliak-Negami element [35]. The overall impedance spectra can then be analysed by an equivalent circuit, given as an insert in Fig. 2. The estimation of the single components has been achieved by CNLS-regression (complex nonlinear least squares regression [36]). As can be seen from Fig. 2, the experimental and calculated spectra agree excellently.

3. Point defect thermodynamics of tephroite

3.1 Tephroite in equilibrium with $MnSiO_3$ resp. MnO (two-phase field)

Taking into account the defects V''_{Mn}, $Mn^{\bullet}_{Mn}$, Mn'_{Si} and e' as majority point defects in accordance with our results on the non-stoichiometry of tephroite [34], we are able to write down the following defect reactions:

$$1/2\ O_2 + 3\ Mn^{\times}_{Mn} + MnSiO_3 = 2\ Mn^{\bullet}_{Mn} + V''_{Mn} + Mn_2SiO_4 \qquad (1)$$

$$1/2\ O_2 + Mn^{\times}_{Mn} + Si^{\times}_{Si} + 2\ Mn_2SiO_4 = Mn'_{Si} + Mn^{\bullet}_{Mn} + 3\ MnSiO_3\ . \qquad (2)$$

The application of the mass-action law leads to expressions for the dependence of the defect concentrations on the independent thermodynamic variables ($a_{Mn_2SiO_4} = 1$ in any case):

$$[Mn_{Mn}^{\bullet}]^2[V_{Mn}''] = K_1 a_{MnSiO_3} a_{O_2}^{1/2} \tag{3}$$

$$[Mn_{Mn}^{\bullet}][Mn_{Si}'] = K_2 a_{MnSiO_3}^{-3} a_{O_2}^{1/2} \tag{4}$$

[ ] designates the site fraction of the defects on their respective sublattice ($[Mn_{Mn}^{\times}] = [Si_{Si}^{\times}] = 1$ for stoichiometric tephroite).

The concentration of electrons depends on the concentration of $Mn_{Mn}^{\bullet}$ defects according to the intrinsic defect equilibrium

$$[Mn_{Mn}^{\bullet}][e'] = K_{el}. \tag{5}$$

The electroneutrality condition reads

$$4\,[V_{Mn}''] + [Mn_{Si}'] + 2\,[e'] = 2\,[Mn_{Mn}^{\bullet}]. \tag{6}$$

It has been assumed that the electrons are located in the cationic sublattice; this explains the factor 2 in front of [e′], $[V_{Mn}'']$ and $[Mn_{Mn}^{\bullet}]$ in the above equation.

With the help of Eqs. (3)−(6) we can express the hole concentrations as function of the independent thermodynamic variables a_{O_2} and a_{MnSiO_3}:

$$[Mn_{Mn}^{\bullet}]^3 = 2\,K_1 \cdot a_{MnSiO_3} \cdot a_{O_2}^{1/2} + \frac{1}{2} K_2 \cdot a_{MnSiO_3}^{-3} \cdot a_{O_2}^{1/2}[Mn_{Mn}^{\bullet}] + K_{el}[Mn_{Mn}^{\bullet}]. \tag{7}$$

Analogous expressions can be derived for $[V_{Mn}'']$ and $[Mn_{Si}']$ as well.

As can been seen from Eq. (7), which describes the dependence of the hole concentration on oxygen activity along the phase boundary Mn_2SiO_4/$MnSiO_3$ with $a_{MnSiO_3} = 1$, numerical calculations will be possible as soon as values for the mass-action law constants K_1, K_2 and K_{el} are available. These calculations will be performed in chapter 4.3.

If we change from tephroite saturated with $MnSiO_3$ ($a_{MnSiO_3} = 1$) to MnO-saturated samples ($a_{MnO} = 1$), we have to calculate the rhodonite activity in tephroite in equilibrium with MnO in order to correctly use Eq. (7) in that case.

Values of the standard Gibbs energy $\Delta G°$ for the tephroite formation reaction from rhodonite and MnO according to

$$MnSiO_3 + MnO = Mn_2SiO_4 \tag{8}$$

are known from the literature [34, 37, 38]. By a least-squares fitting procedure we received the relationship

$$\Delta G_8^0 = \left(-38{,}300 + \frac{14.8\,T}{K}\right) J\,mol^{-1} \tag{9}$$

which we used in our calculations.

3.2 Tephroite within the one-phase field

In order to derive a relation between the hole concentration and oxygen activity within the tephroite one-phase field (which approximately coincides with stoichiometric composition), we first combine the chemical reaction Eqs. (1) and (2) by eliminating $MnSiO_3$; this yields:

$$10\,Mn_{Mn}^{\times} + Si_{Si}^{\times} + 2\,O_2 = Mn_2SiO_4 + Mn_{Si}' + 3\,V_{Mn}'' + 7\,Mn_{Mn}^{\bullet}. \quad (10)$$

The mass-action law for Eq. (10) reads

$$[Mn_{Mn}^{\bullet}]^7[V_{Mn}'']^3[Mn_{Si}'] = K_1^3\,K_2\,a_{O_2}^2\,. \quad (11)$$

The mass-action law for the (intrinsic) electronic defect equilibrium, which is valid indepenent of oxygen activity is given as

$$[Mn_{Mn}^{\bullet}][e'] = K_{el}\,. \quad (12)$$

To solve for the four defect concentrations $[Mn_{Mn}^{\bullet}]$, $[V_{Mn}'']$, $[Mn_{Si}']$ and $[e']$ we need two more equations. One of these is the electroneutrality condition

$$2\,[Mn_{Mn}^{\bullet}] = 4\,[V_{Mn}''] + [Mn_{Si}'] + 2\,[e']\,. \quad (13)$$

The other one we are looking for can be taken from Eq. (10), from which the following relation between the concentration of defects $[V_{Mn}'']$ and $[Mn_{Si}']$ emerges in case that tephroite is stoichiometric in composition:

$$[Mn_{Si}'] = \frac{2}{3}\,[V_{Mn}'']\,. \quad (14)$$

Because of the validity of the (intrinsic) electronic defect equilibrium Eq. (12), no other relations between defect concentrations can be deduced from Eq. (10). Solving Eqs. (11)–(14) for $[Mn_{Mn}^{\bullet}]$, we arrive at

$$[Mn_{Mn}^{\bullet}]^3 = \frac{7}{3}\left(\frac{3}{2}\right)^{1/4}(K_1^3\,K_2)^{1/4}a_{O_2}^{1/2}[Mn_{Mn}^{\bullet}]^{1/4} + K_{el}[Mn_{Mn}^{\bullet}]\,. \quad (15)$$

We have to emphasize that Eq. (15) is appliceable within the whole oxygen activity range we covered in our experiments.

Concerning the hole concentration dependence on oxygen activity within the tephroite one-phase field at only high activities, we go back to Eq. (13). Because the concentration of electrons at high oxygen activities is to be considered as neglegible small, the electroneutrality condition Eq. (13) reduces to

$$2\,[Mn_{Mn}^{\bullet}] = 4\,[V_{Mn}''] + [Mn_{Si}']\,. \quad (16)$$

Taking into account Eq. (14), we yield a second relation between the concentration of defects within the tephroite one-phase field, that is

$$[Mn_{Mn}^{\bullet}] = \frac{7}{3}\,[V_{Mn}'']\,. \quad (17)$$

This relationship can also directly be derived from Eq. (10) within the high-oxygen region remembering the fact, that mole fractions, designated as ( ) and site fractions [ ] are linked by a factor of 2 for Mn-lattice sites in tephroite, $(Mn^{\bullet}_{Mn}) = 2\,[Mn^{\bullet}_{Mn}]$ for instance. Inserting Eqs. (14) and (17) into Eq. (11) we arrive at

$$[Mn^{\bullet}_{Mn}] = \left(\frac{7}{2}\right)^{1/11}\left(\frac{7}{3}\right)^{3/11}(K_1^3\,K_2)^{1/11}\,a_{O_2}^{1/5.5}\,. \tag{18}$$

As can be seen from Eq. (18) the hole concentration has to obey an 1/5.5-power law as function of the oxygen activity in case that our model is correct. According to Eq. (17) the same is true for the vacancy concentration $[V''_{Mn}]$. It was exactly this 1/5.5-power law which we derived from our measurements of the nonstoichiometry δ of tephroite $(Mn,Si)_{3-3\delta}O_4$ as a function of oxygen activity [34].

At this point we have to emphasize that no defect associates appear in our defect model developed so far in contrast to $\{Fe^{\bullet}_{Fe}\,Fe'_{Si}\}^{x}$ associates, which play an important role in the model depicted by Nakamura and Schmalzried for fayalite [1]. Consequently, it seems quite reasonable to tentatively interprete the conductivity results described in this paper by only utilizing $Mn^{\bullet}_{Mn}$, V''_{Mn}, Mn'_{Si} and e' as majority defects.

4. Data analysis

4.1 Separation of partial conductivities from overall conductivities

The electrical conductivity of an electronic conductor is given as the sum of the partial conductivities σ_e and σ_h of electrons and holes

$$\sigma = \sigma_e + \sigma_h\,. \tag{19}$$

In our case the concentration of holes is identical with the concentration of the $Mn^{\bullet}_{Mn}$-defect species, which leads to the following expression for the total electrical conductivity

$$\sigma = \frac{2F}{V_m}\,(u_e[e'] + u_h[Mn^{\bullet}_{Mn}]) \tag{20}$$

F = Faraday's constant, V_m = molar volume of tephroite, u = electrochemical mobility.
Using the abbreviation

$$f_i = \frac{2F}{V_m}\cdot u_i \qquad i = e,h \tag{21}$$

Eq. (20) reads

$$\sigma = f_e[e'] + f_h[Mn^{\bullet}_{Mn}] . \tag{22}$$

In the following section it will be shown, how the hole conductivity σ_h can be separated from the total conductivity σ in case that σ passes a minimum in dependence on the oxygen activity.

First, Eq. (12) is multiplied through by the product $f_e f_h$ (see Eq. (21)); one gets

$$\sigma_e \cdot \sigma_h = K_{el} \cdot f_e \cdot f_h = \tilde{K}^0. \tag{23}$$

Insertion into Eq. (19) yields

$$\sigma = \sigma_h + \frac{K_{el} f_e f_h}{\sigma_h} . \tag{24}$$

Because Eq. (23) is valid without any restrictions, it must hold for the conductivity minimum itself, that is (minimum values are marked by an upper zero index)

$$\sigma_e^0 \sigma_h^0 = K_{el} f_e^0 f_h^0. \tag{25}$$

At the minimum of σ both partial conductivities are equal; thus we have

$$\sigma_h^0 = \sigma_e^0 = \frac{\sigma^0}{2} . \tag{26}$$

Introducing this into Eq. (21), we find

$$\left(\frac{\sigma^0}{2}\right)^2 = K_{el} f_e^0 f_h^0. \tag{27}$$

In a strict sense, this expression is valid only at the minimum of σ. In a zero'th order approximation we assume that the hole mobility u_h and the mobilit u_e of electrons as well are independent on oxygen activity. Based on this assumption Eq. (27) alters into

$$\left(\frac{\sigma^0}{2}\right)^2 = K_{el} f_e f_h . \tag{28}$$

Combining the last expression with Eq. (24), we finally have

$$\sigma = \sigma_h + \frac{\left(\frac{\sigma^0}{2}\right)^2}{\sigma_h} . \tag{29}$$

The possibility to separate hole conductivities σ_h from overall conductivities σ according to Eq. (29) will enormously facilitate the mathematical procedure in getting values for the equilibrium constants Eqs. (3)–(5) as will be shown in section 4.3.

4.2 Electrical conductivity and point-defect concentrations

Expressions for the dependence of hole conductivities on oxygen activities can easily be obtained from Eq. (7), which is valid for the two-phase region of tephroite ($MnSiO_3$ resp. MnO saturation) and from Eq. (15) or Eq. (18) for the one-phase region, where the latter is valid only at high oxygen activities, on the basis of the following equation

$$\sigma_h = \frac{F}{V_m} u_h [Mn^{\bullet}_{Mn}] \tag{30}$$

Eq. (30) is inherent in Eq. (20) as well.

The expression for the two-phase region reads (see Eq. (7)):

$$\sigma_h^3 = 2\,\tilde{K}_1 \cdot a_{MnSiO_3} \cdot a_{O_2}^{1/2} + \frac{1}{2}\,\tilde{K}_2 \cdot a_{MnSiO_3}^{-3} \cdot a_{O_2}^{1/2} \sigma_h + \tilde{K}_{el}\,\sigma_h. \tag{31}$$

The abbreviations used in Eq. (31) have the following meaning (see Eq. (21))

$$\tilde{K}_1 = K_1 \cdot f_h^3 \tag{32}$$

$$\tilde{K}_2 = K_2 \cdot f_h^2 \tag{33}$$

$$\tilde{K}_{el} = K_{el} \cdot f_h^2 . \tag{34}$$

We arrive at an expression analogous to Eq. (31), which is valid within the one-phase field over the whole oxygen activity range via Eqs. (15) and (30), which is not given here. The expression for the one-phase field at exclusively high oxygen activities (see Eq. (18)) is:

$$\sigma_h = \left(\frac{7}{2}\right)^{1/11} \left(\frac{7}{3}\right)^{3/11} (\tilde{K}_1^3\,\tilde{K}_2)^{1/11}\, a_{O_2}^{1/5.5}. \tag{35}$$

4.3 Mathematical procedure

In order to estimate values for $\tilde{K}_1$, $\tilde{K}_2$, $\tilde{K}_{el}$ and σ^0 from our experimental $\sigma = f(a_{O_2})$ data and to be able to subsequently calculate $\sigma = f(a_{O_2})$ plots, we proceeded as follows.

The most straightforward way to solve this problem would have been to insert expressions for σ_h (Eq. (31) for instance) and the analogous one for σ_e (not given here) into Eq. (19) and trying to find the above mentioned parameters by an appropriate fitting procedure. However, because it was too hard a task to handle the bulky mathematics properly we have choosen

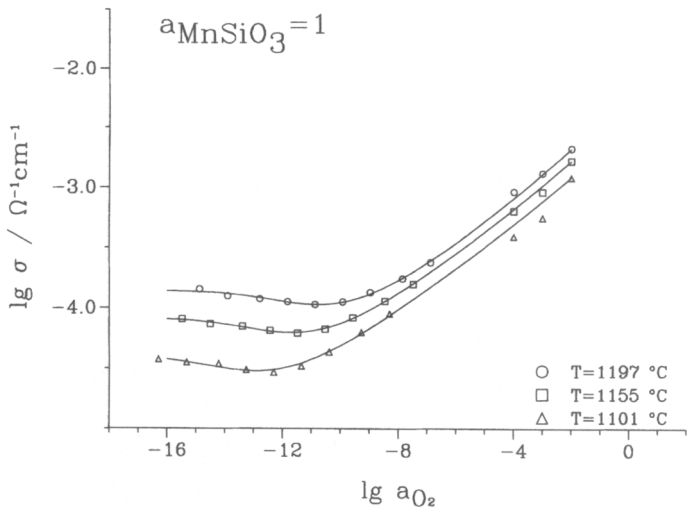

Fig. 3. Specific electrical conductivity of tephroite as a function of the oxygen activity at 1197, 1101, and 1155°C. The MnO activity is fixed at $a_{MnSiO_3} = 1$. Calculated values are given as full lines (see chapter 5).

another way of finding reliable values for $\tilde{K}_1$, $\tilde{K}_2$, $\tilde{K}_{el}$ and σ^0 via a method, in which only σ_h is involved instead of both the partial conductivities σ_h and σ_e.

First, values for σ^0, the minima values of the overall conductivities σ were deduced by spline interpolation from experimental data. These first values for σ^0, which themselves will then be included in the fitting procedure described below, were used to separate σ_h values from the σ's according to Eq. (29).

Afterwards, we performed a transformation of variables with σ_h, which enabled us via a weighted polynomial regression to find a first set of the constants $\tilde{K}_1$, $\tilde{K}_2$ and $\tilde{K}_{el}$ by linear regression. The calculation of σ_h from Eq. (31) could then be carried out by an iteration procedure from the roots of Eq. (31).

The next step was a non-linear regression of the experimental σ values according to the Gauß-Newton procedure. Because we are looking for an explicit solution of Eq. (31) in order to solve the deviation matrix (Jacobi matrix), the non-linear regression procedure is not directly applicable. Therefore we were forced in a preceding step to solve Eqs. (29) and (31) numerically by simultaneous minimization. This way, values for σ and all the other mathematical parameters (deviations such as $\delta\tilde{K}_i/\delta\sigma$ for instance) were calculable in consecutive iterations as soon as this starting set for $\tilde{K}_1$, $\tilde{K}_2$ and $\tilde{K}_{el}$ was available.

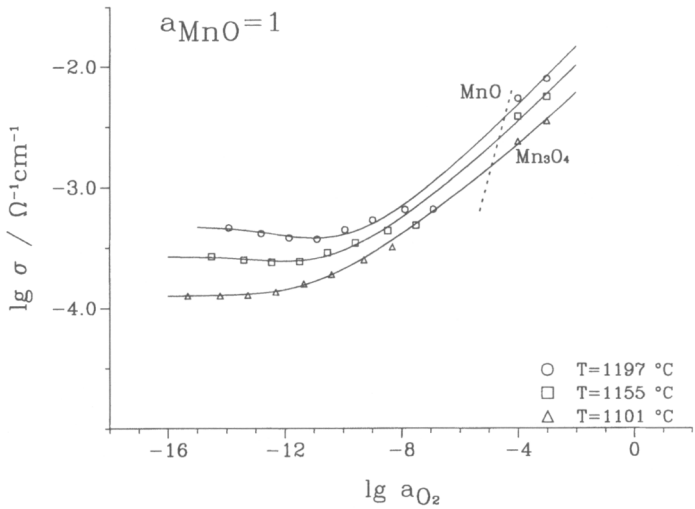

Fig. 4. Specific electrical conductivity of tephroite as a function of the oxygen activity at 1197, 1101, and 1155°C. The MnO activity is fixed at $a_{MnO} = 1$. Calculated values are given as full lines (see chapter 5). The MnO/Mn_3O_4-phase boundary is indicated by a broken line.

5. Results

For all our samples $(Mn,Si)_{3-3\delta}O_4$, i.e. independent on composition we found a minimum for the electrical conductivity (overall conductivity) in dependence on oxygen activity. Characteristic examples for these dependencies are given in Figs. 3–5.

The minima are well-defined in samples with silicon excess ($a(MnSiO_3) = 1$); they are less pronounced in both the other cases ($a(MnO) = 1$; $n(Mn)/n(Si) = 2$, stoichiometric).

From the existence of the minima we conclude that p-type conduction prevails at high oxygen activities ($a_{O_2} > a^0_{O_2}$) whereas the samples become n-type conducting at lower oxygen activities ($a_{O_2} < a^0_{O_2}$).

In all cases an excellent agreement is obtained between experimental points and curves calculated as outlined in the foregoing section.

Values for $\tilde{K}_1$, $\tilde{K}_2$ and $\tilde{K}_{el}$, which emerged from our fitting procedure are listed for $T = 1155$°C and $T = 1197$°C in Table 1. Included in Table 1 are values for $\tilde{K}_1^3\,\tilde{K}_2$ and $\tilde{K}^0$, which will be of some importance in the discussion given below. The agreement between values calculated on the basis of data, given in Table 1 and experimental values is excellent (Figs. 3–5).

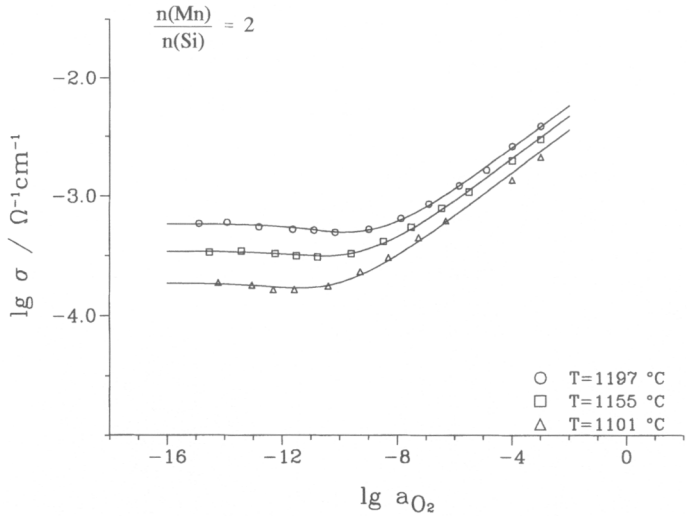

Fig. 5. Specific electrical conductivity of tephroite as a function of the oxygen activity at 1197, 1101, and 1155°C. The tephroite samples are stoichiometric in composition (n(Mn)/n(Si) = 2).

Table 1. Mass-action-law constants calculated from the experimental values of the specific electrical conductivity of tephroite (see chapter 4.3).

		$a_{MnO} = 1$	$\frac{n(Mn)}{n(Si)} = 2$	$a_{MnSiO_3} = 1$
1197°C	lg $\tilde{K}_1$	−5.64±0.21	−6.02±0.05*	−7.85±0.04
	lg $\tilde{K}_2$	−4.15±0.07		−4.22±0.06
	lg $\tilde{K}_1^3 \tilde{K}_2$	−21.06±0.70	−22.26±0.09	−27.77±0.18
	lg $\tilde{K}_{el}$	−8.04±0.29	−7.70±0.07	−9.20±0.04
	lg $\tilde{K}^0$	−7.44±0.05	−7.21±0.02	−8.55±0.02
1155°C	lg $\tilde{K}_1$	−5.93±0.21	−6.29±0.05*	−8.07±0.02
	lg $\tilde{K}_2$	−4.29±0.07		−4.45±0.04
	lg $\tilde{K}_1^3 \tilde{K}_2$	−22.09±0.70	−23.24±0.08	−28.67±0.11
	lg $\tilde{K}_{el}$	−8.09±0.29	−7.97±0.09	−9.64±0.05
	lg $\tilde{K}^0$	−7.81±0.04	−7.61±0.02	−9.01±0.01

* Calculated with a mean value of $\tilde{K}_2$.

6. Discussion

As can be seen from chapter 3, our defect model is based on the assumption that only the four species V''_{Mn}, $Mn^{\bullet}_{Mn}$, Mn'_{Si} and e' are of any importance in depicting the defect structure of tephroite.

Table 2. Values for the exponent n in $\log \sigma \sim (1/n)\log a_{O_2}$ for different majority defects in tephroite which is in equilibrium with the phases indicated in the upper row (n(Mn)/n(Si)) = 2 means "stoichiometric").

	Mn	MnO	Mn_3O_4	$MnSiO_3$	$\frac{n(Mn)}{n(Si)} = 2$
V''_{Mn}, $Mn^{\bullet}_{Mn}$	0	1/6	1/4.5	1/6	1/5.5
Mn'_{Si}, $Mn^{\bullet}_{Mn}$	1	1/4	0	1/4	
$\{Mn'_{Si}\ Mn^{\bullet}_{Mn}\}^x$	0	1/6	1/4.5	1/6	1/5.0

Supported by the good agreement between experiment and theory we conclude that our point-defect model which allows for defect species V''_{Mn}, $Mn^{\bullet}_{Mn}$, Mn'_{Si} and e' has a realistic meaning. Defect associates, which may be formed according to the defect reaction

$$Mn^{\bullet}_{Mn} + Mn'_{Si} = \{Mn^{\bullet}_{Mn}Mn'_{Si}\}^x \tag{36}$$

are not included in our model. If such defect associates would actually exist in tephroite in analogy to fayalite $\{Fe^{\bullet}_{Fe}\ Fe'_{Si}\}^x$ [1], the slope of the log σ-log a_{O_2} plots had to be 1/5.0 for stoichiometric tephroite (n(Mn)/n(Si) = 2) in the range of high oxygen activities, whereas we found an 1/5.5-power law in accordance with Eq. (35). In case of MnO- resp. $MnSiO_3$-saturated samples we would expect an 1/6-power dependence of σ from a_{O_2} if associates were present as a majority defect (see Table 2); however, we could not verify this value in our experiments.

Having in mind that we have not taken into account defect species on interstitial sites such as $Mn_i^{\bullet\bullet}$ or $Si_i^{\bullet\bullet\bullet\bullet}$ we have to give an explanation why these defects have been ruled out from our model. First of all it is well established that cation diffusion in olivine-type silicates proceeds via vacancies. That means Mn^{2+}-cations on interstitial sites can at best be regarded as minority defects; but it is not possible to draw any conclusions about minority defects from our conductivity measurements. As will be seen from a forthcoming paper [34] results from coulometric titration experiments can consistently be interpreted without postulating the existence of interstitial Mn^{2+}-ions as a majority defect. In addition it follows from the literature [37] that even in MnO investigated by thermogravimetry, Mn^{2+} interstitials are of no importance.

Similar arguments can advanced concerning Si^{4+} on interstitial positions. In accordance with Nakamura and Schmalzried [1] we consider from a mere chemical viewpoint Si^{4+}-interstitials as the energetically most

unfavourable defect species in olivine. Moreover it is not possible to establish an 1/5.5-power dependence of $[V''_{Mn}]$ or $[Mn^{\bullet}_{Mn}]$ (see Eq. (35)) taking into account $Si_i^{\bullet\bullet\bullet\bullet}$ in addition to V''_{Mn} and $Mn^{\bullet}_{Mn}$ as a majority defect.

Values for $\tilde{K}_i$ (i = 1, 2, el) and $\tilde{K}^0$ at T = 1155 and 1197 °C are listed in Table 1.

Whereas $\tilde{K}_2$ is independent of composition as expected, $\tilde{K}_1$ decreases with decreasing MnO content by about two orders of magnitude. The decrease can be explained only by assuming that an MnO excess in tephroite enhances the hole mobility which on the other hand raises the values for $\tilde{K}_1$ according to Eq. (32).

We have some other evidence that the hole mobility does actually depend on the MnO concentration of tephroite. Obviously values for $\tilde{K}_{el}$ also increase with increasing MnO content although not as much as is the case with $\tilde{K}_1$. Furthermore, we observe a shift (see Figs. 3–5) of the σ^0 values to lower oxygen potentials with increasing MnO content. That means that according to the higher mobility of holes at higher MnO contents the condition for the minimum in the $\ln \sigma = f(\ln a_{O_2})$ curves

$$\sigma_e = \sigma_h \tag{37}$$

resp.

$$u_e \cdot [e'] = u_h \cdot [Mn^{\bullet}_{Mn}] \tag{38}$$

is already realized at lower $Mn^{\bullet}_{Mn}$-concentrations.

In order to obtain values for the hole mobilities from our estimations of $\tilde{K}_1$ and $\tilde{K}_2$, we have to refer to the equilibrium constants K_1 and K_2 derived from our coulometric titration experiments [34]. At 1197 °C we obtained $\log K_1 = -7.120$ and $\log K_2 = -4.182$. This leads to $u_h = 4.8 \cdot 10^{-4}$ cm²/Vs resp. $5.8 \cdot 10^{-4}$ cm²/Vs; the mean value is $5.3 \cdot 10^{-4}$ cm²/Vs.

The product $K_1^3 K_2$ of the equilibrium constants was found to be independent of temperature by the authors cited above. Hence we have to attribute the temperature dependence of $\tilde{K}_1^3 \tilde{K}_2$ estimated from our conductivity measurements (see Table 1) to the temperature dependence of the hole mobility itself which is inherent in the product $\tilde{K}_1^3 \tilde{K}_2$. Consequently it must be possible to deduce the temperature dependence of the hole mobility from an Arrhenius plot of $\tilde{K}_1^3 \tilde{K}_2$ versus $1/T$ (see Fig. 6); the estimated value for the activation energy from this plot is $E_{A_h} = 0.85$ eV.

In Table 3 we compare our results concerning the hole mobility of tephroite with the hole mobilities of other olivines and their relevant binary component oxides. Most striking is the fact that the extremely low value for the hole mobility of tephroite in the series Co_2SiO_4, Fe_2SiO_4, Mn_2SiO_4 seems to reflect the low value for the hole mobility in MnO in the series CoO, FeO, MnO. Our results for u_h and E_h clearly suggest a hopping mechanism (small polaron mechanism) for the electronic conductivity of tephro-

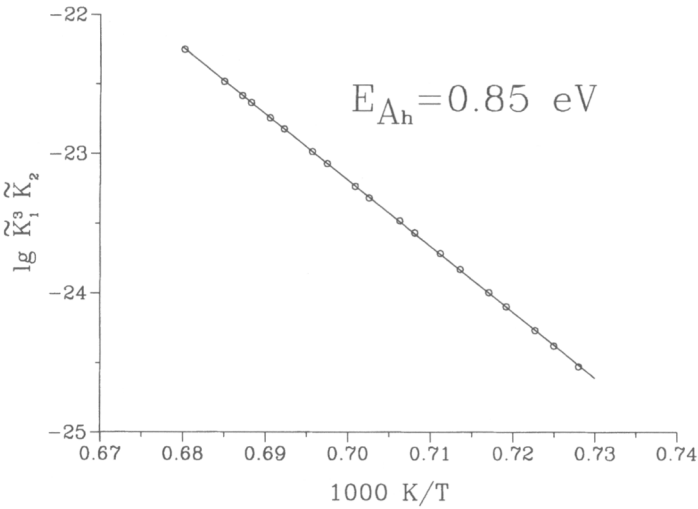

Fig. 6. Temperature dependence of the mass-action constants product $\tilde{K}_1^3 \tilde{K}_2$. The slope of the straight line is determined by the temperature dependence of the charge carrier mobility (see text).

Table 3. Comparison of hole mobilities for some binary oxides and ternary silicates of some 3d-transition metals.

Compound	u_h / $cm^2V^{-1}s^{-1}$	T / °C	Ref.
Co_2SiO_4	$7 \cdot 10^{-2}$	1100	[21]
Fe_2SiO_4	$6 \cdot 10^{-3}$	1150	[22]
Mn_2SiO_4	$6 \cdot 10^{-4}$	1200	this work
CoO	0.3	1150	[21]
FeO	0.2	1200	[22]
MnO	$3 \cdot 10^{-2}$	1150	[38]

ite. Combining the values for u_h and $\tilde{K}_{el}$ we estimate a value for K_{el}, the equilibrium constant for the (intrinsic) electronic equilibrium (see Eq. (12)); this yields $\log K_{el} = -8.43$ at 1197°C.

By use of our value for K_{el} and along with the values for K_1 and K_2 taken from [34] we are able to calculate the concentration of the defect species V''_{Mn}, Mn'_{Si}, $Mn^{\bullet}_{Mn}$ and e' as function of the oxygen activity with the help of expressions derived from Eqs. (3)−(6) for the two-phase field and from Eqs. (11)−(14) for the one-phase field.

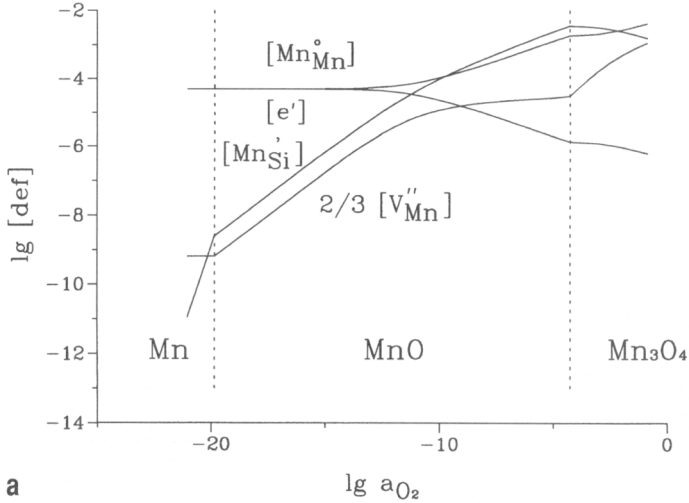

Fig. 7a. Kröger-Vink diagram for tephroite at 1197°C calculated for activities fixed at $a_{Mn} = 1$, $a_{MnO} = 1$ resp. $a_{Mn_3O_4} = 1$. Two-phase boundaries are marked by broken lines. The end points of the curves correspond to the three-phase equilibria $Mn/MnSiO_3/Mn_2SiO_4$ (left) and $Mn_3O_4/MnSiO_3/Mn_2SiO_4$ (right).

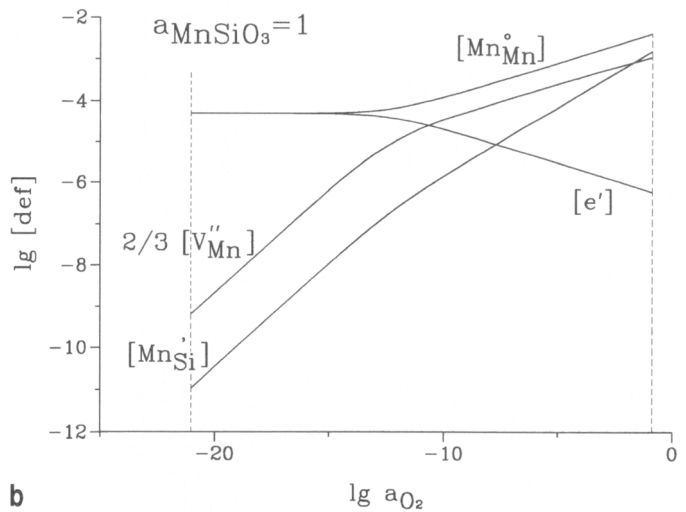

Fig. 7b. Kröger-Vink diagram for tephroite at 1197°C calculated for fixed $MnSiO_3$ activity ($a_{MnSiO_3} = 1$). The broken lines correspond to three-phase equilibria $Mn/MnSiO_3/Mn_2SiO_4$ (left) resp. $Mn_3O_4/MnSiO_3/Mn_2SiO_4$ (right).

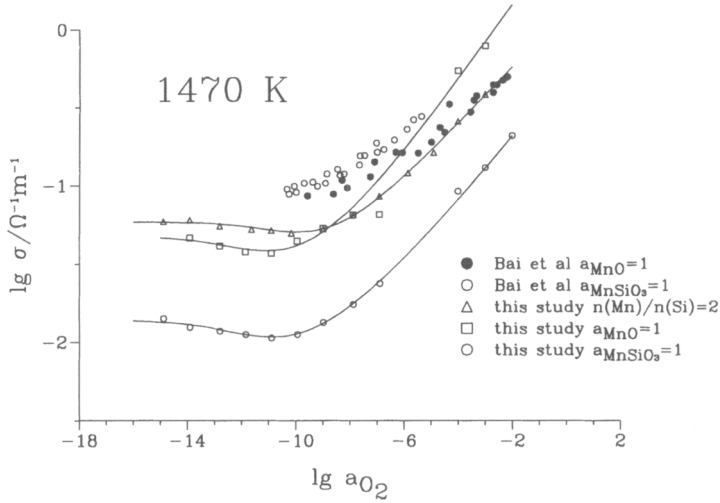

Fig. 8. Comparison of the oxygen-activity dependence of the electrical conductivity of tephroite (this work) with literature data according to [30].

The calculation has been carried out at $T = 1197\,°C$ for both the tephroite phase in equilibrium with Mn, MnO or Mn_3O_4 on the one hand (Fig. 7a) and the tephroite phase in equilibrium with $MnSiO_3$ (Fig. 7b) on the other hand.

As can be seen from Fig. 7a, tephroite exists with a manganese excess ($[Mn'_{Si}] > \frac{2}{3}[V''_{Mn}]$) all over the two-phase equilibrium tephroite/MnO. The stoichiometric composition ($[Mn'_{Si}] = \frac{2}{3}[V''_{Mn}]$) is approached only at very low oxygen activities ($a_{O_2} \approx 10^{-20}$) where tephroite is in equilibrium with metallic manganese.

Along the two-phase equilibrium tephroite/$MnSiO_3$ we observe an excess of silicon not only at medium values of oxygen activities but also down to very low values. Even at $a_{O_2} = 10^{-20}$ tephroite in equilibrium with $MnSiO_3$ exists with an excess of silicon ($[Mn'_{Si}] < \frac{2}{3}[V''_{Mn}]$).

A second 'critical' oxygen activity exists in Figs. 7a and 7b at which a stoichiometric composition ($[Mn'_{Si}] = \frac{2}{3}[V''_{Mn}]$) is established in tephroite in equilibrium with Mn_3O_4 and $MnSiO_3$ respectively at about $a_{O_2} = 10^{-1}$ and $a_{O_2} = 10^{-2}$. However these points are located outside the oxygen potential range, wherein tephroite is thermodynamically stable and therefore is of no concern to our foregoing discussion.

To our knowledge only one paper can be found in the literature [30] which deals with the electrical conductivity of tephroite measured under conditions comparable to the ones described above. Another paper concerning the same subject is being prepared by Dieckmann [41].

The results of Bai *et al.* [30] are included together with our own results in Fig. 8. These authors found the electrical dc-conductivity, measured by two-point method to be about 2.5 times faster along [100] than along [010]. A similar behaviour is known from diffusion experiments in olivines [11, 14], where diffusion coefficients decrease from crystallographic c- to a- to b-direction. Because polycrystalline samples have been used in our measurements a straightforward comparison between Bai's conductivities and ours is not possible. Nevertheless two things have to be commented. First of all we have to look at the dependence of σ from MnO- resp. $MnSiO_3$ activity. Bai *et al.* found that activities have only a small effect on conductivities with $MnSiO_3$-saturated samples showing about 1.6 times higher values than MnO-saturated ones. By contrast we found that conductivities of MnO-saturated samples are about 6 times higher than conductivities of $MnSiO_3$-saturated ones. Secondly, a conductivity minimum could not be detected by Bai *et al.* which is not that surprising because these authors restricted their measurements to oxygen activities as low as only 10^{-10}, whereas our measurements were carried out down to about 10^{-16}.

The defect model, developed by Bai *et al.* differs in so far from our model as these authors take into account only three majority defects which are $Mn_{Mn}^{\bullet}$, V_{Mn}'' and e' whereas our model is based on a fourth majority defect that is Mn_{Si}'. In agreement with our results (see Fig. 7a and 7b) Bai *et al.* propose that the charge neutrality condition switches from $[Mn_{Mn}^{\bullet}] = [e']$ at low activities to $[Mn_{Mn}^{\bullet}] = 2\,[V_{Mn}'']$ at high activities. Concerning the conduction mechanism at high oxygen activities, Bai *et al.* give a somewhat different interpretation of their results in so far as they assume that conductivities at high temperatures are carried completely by transport of Mn^{2+} ions via vacancies, whereas hopping motion of $h^{\bullet}$ is responsible for conduction at low temperature. In contrast to our experiments, Bai *et al.* have not been able to estimate values for the mass action constants of the predominating defect equilibria, which we did because we could combine our results given here with our results from coulometric titration experiments, which will be published soon [34].

Acknowledgement

This work was financed by the Deutsche Forschungsgemeinschaft, which is greatly appreciated.

References

1. A. Nakamura and H. Schmalzried, Phys. Chem. Minerals **10** (1983) 27–37.
2. H. Annersten, J. Adetunji and A. Filippidis, Am. Min. **69** (1984) 1110–1115.

3. H. Schmalzried, Phys. Chem. Minerals **2** (1978) 279–294.
4. H. Schmalzried, *Chemical Kinetics of Solids*, 433 pp., VCH, Weinheim, Germany (1995).
5. D. M. Smyth and R. L. Stocker, Phys. Earth Planet. Inter. **10** (1975) 183–192.
6. R. L. Stocker and D. M. Smyth, Phys. Earth Planet. Inter. **16** (1978) 145–156.
7. R. L. Stocker, Phys. Earth Planet. Inter. **17** (1978) 108–117.
8. R. L. Stocker, Phys. Earth Planet. Inter. **17** (1978) 118–129.
9. D. L. Ricoult and D. L. Kohlstedt, Geophys. Monogr. **31** (1985) 171–184.
10. D. L. Ricoult and D. L. Kohlstedt, Philos. Mag. A **51** (1985) 79–93.
11. J. Hermeling and H. Schmalzried, Phys. Chem. Minerals **11** (1984) 161–166.
12. A. Nakamura and H. Schmalzried, Ber. Bunsenges. Phys. Chem. **88** (1984) 140–145.
13. K. Andersson, G. Borchardt, O. Müller and G. Róg: In Vinzenzine, P. (ed.), *High Tech. Ceramics,* Elsevier, Amsterdam (1987) 329–340.
14. M. Morioka and H. Nagasawa, Adv. Phys. Geochem. **8** (1991) 176–197.
15. K. D. Becker, S. Dreher and S. Wißmann, Ber. Bunsenges. Phys. Chem. **96** (1992) 1778–1783.
16. U. Brinkmann and W. Laqua, Phys. Chem. Minerals **12** (1985) 283–290.
17. J. Wolfenstine, D. Dimos and D. L. Kohlstedt, J. Am. Ceram. Soc. **1985**, C117-C118.
18. U. Brinkmann and W. Laqua, Ber. Bunsenges. Phys. Chem. **90** (1986) 680–684.
19. G. Schwier, R. Dieckmann and H. Schmalzried, Ber. Bunsenges. Phys. Chem. **77** (1973) 402–408.
20. A. Duba and I. A. Nicholls, Earth Planet. Sci. Letters **18** (1973) 59–64.
21. G. Schwier and H. Schmalzried, Ber. Bunsenges. Phys. Chem. **77** (1973) 721–726.
22. H. G. Sockel, *Defects and Transport in Oxides*, N. S. Schmelzer and R. J. Jaffe, eds., Plenum Press, New York (1974) 341–355.
23. C. Greskovich and H. Schmalzried, J. Phys. Chem. Solids **31** (1970) 639–646.
24. B. J. Wanamaker and A. G. Duba, J. Geophys. Res. **98** (1993) 489–500.
25. L. Cemič, G. Will and E. Hinze, Phys. Chem. Minerals **6** (1980) 95–107.
26. R. N. Schock and A. G. Duba, Geophys. Monogr. **31** (1985) 88–96.
27. R. N. Schock, A. G. Duba and T. J. Shankland, J. Geophys. Res. **94** (1989) 5829–5839.
28. L. M. Hirsch, Phys. Chem. Minerals **17** (1990) 187–190.
29. S. Constable and A. G. Duba, J. Geophys. Res. **95** (1990) 6967–6978.
30. Q. Bai, Z.-C. Wang and D. L. Kohlstedt, Phys. Chem. Minerals **22** (1995) 489–503.
31. C. Stüber and W. Laqua, Ber. Dt. Min. Ges. **1** (1990) 256.
32. Th. Barkmann and L. Cemič, Phys. Chem. Minerals **23** (1996) 186–192.
33. A. Lacam, Phys. Chem. Minerals **12** (1985) 23–28.
34. R. Sandner and W. Laqua, in preparation.
35. J. R. McDonald and L. D. Potter, Solid State Ionics **23** (1987) 61–79.
36. J. R. McDonald, North Carolina State University, Chapel Hill (1990).
37. A. Navrotsky, J. Inorg. Nucl. Chem. **33** (1971) 4035–4050.
38. C. Stüber, Thesis, University of Giessen, Germany (1993).
39. M. Keller and R. Dieckmann, Ber. Bunsenges. Phys. Chem. **89** (1985) 883–893.
40. N. G. Eror and J. B. Wagner, J. Electrochem. Soc. **118** (1971) 1665–1670.
41. R. Dieckmann, private communication.